AFM characterization of cellulose nanocrystal height and width using internal calibration standards

Chen, Maohui; Parot, Jeremie; Hackley, Vincent A.; Zou, Shan; Johnston, Linda J.

Publisher's version / Version de l'éditeur:
https://doi.org/10.1007/s10570-021-03678-0
Cellulose, 28, 4, pp. 1933-1946, 2021-01-26

AFM Characterization of Cellulose Nanocrystal Height and Width Using Internal Calibration Standards

Maohui Chen,[1] Jeremie Parot,[2] Vincent A. Hackley,[2] Shan Zou,[1] Linda J. Johnston[1]

[1]Metrology Research Center, National Research Council Canada, Ottawa, ON, K1A 0R6, Canada

[2]National Institute of Standards and Technology, Gaithersburg, MD 20899-8520, USA

Abstract. A variety of models have been suggested for the cross-sectional shape and dimensions of cellulose nanocrystals (CNCs). Although many studies report measurements of CNC width (from transmission electron microscopy, TEM) and height (from atomic force microscopy, AFM), few have measured both cross-sectional dimensions for the same CNC sample and the same particles. Previous work has demonstrated that the TEM width is approximately twice the AFM height, a result that was explained by lateral aggregation of CNCs. Here we examine this question in more detail by measuring both CNC width and height by a single technique, AFM. The ability to measure both cross-sectional dimensions was facilitated by several factors: access to a fractionated CNC sample with few agglomerated particles, AFM imaging at low applied force with a small, nominal probe radius and in situ calibration of the AFM probe radius using co-deposited gold nanoparticles (AuNPs). Two sizes of AuNPs provided optimal calibration of the tip radius and allowed internal validation of the approach. The results show that the CNC width/height ratio covers a relatively wide range with a larger variation in width than height. The ratios indicate that approximately a third of the particles adsorb with their longer cross-sectional side on the surface. A fraction of CNCs (28 %) have an approximately symmetric cross-section whereas the remainder are asymmetric with one axis that is 2-3 times longer than the other. The results are consistent with the formation of a large fraction of laterally aggregated CNCs that cannot be resolved as individual particles. This has important implications for applications in which the particle length/cross-section determines the CNC properties.

Keywords: Cellulose Nanocrystals; Atomic force microscopy; Gold nanoparticles, Aspect Ratio

Introduction

Cellulose nanocrystals (CNCs) are generated from a renewable natural resource and their novel properties, facile surface modification, increasing commercial production and anticipated minimal toxicity have led to many applications [1-7]. Measurement of CNC particle size distributions requires reproducible methods to disperse the dry material and methods to minimize particle agglomeration/aggregation for microscopy measurements [8, 9]. While characterizing a cellulose nanocrystal certified reference material ("CNCD-1", National Research Council Canada), we optimized methods to measure CNC size distributions by atomic force microscopy (AFM) and transmission electron microscopy (TEM). This work showed that the mean AFM height of individual CNCs was ≈ half the TEM width [10-12]. This result was somewhat surprising since models for CNCs derived from wood pulp have indicated that the CNC cross-section has two axes with similar dimensions [5]. It was hypothesized that the difference between TEM width and AFM height was due to a higher degree of lateral aggregation of CNCs after deposition for TEM and/or an inability to detect CNC aggregation by AFM due to tip convolution effects. There are very few studies in which both AFM height and TEM width have been measured for the same sample of CNCs. In one case, CNCs derived from cotton were shown to have an asymmetric cross-section with width and height of 27 nm and 7.3 nm, respectively, a result that was attributed to aggregation of elementary crystallites [13]. Several other studies have measured TEM width and AFM height for CNCs from a range of plant-based cellulose sources and observed that the height was typically smaller than the width, with the difference ranging from ≈ 20 % to ≈ 200 % [14, 15]. In another example AFM was used to measure both width and height for wood pulp CNCs; the width was approximately 20% larger than the height. To the best of our knowledge, this is the only example in which particle size distributions for both width and height were measured for the same particles [16].

Recently, we had applied previously optimized multi-detector asymmetrical-flow field-flow fractionation (MD-AF4) methods to fractionate CNCD-1 [17, 18]. Multiple fractions were analyzed by both AFM and TEM, with a focus on correlating the AF4 data with microscopy measurements of particle size [18]. The results demonstrate that it is possible to obtain fractionated CNC samples that contain very few clusters (over 90% being single CNCs for the

first AF4 fraction based on AFM measurements), compared to the initial suspension prior to fractionation. This indicates that the agglomeration and an aggregation that is detected by microscopy probably reflects a combination of pre-existing aggregates in the initial suspension and clusters that form during the sample deposition process. However, the average CNC width (7.5 nm) for this primarily single CNC sample, measured by TEM, is still approximately twice the average AFM height (3.2 nm), as observed previously for the unfractionated sample (CNCD-1 [11]). The length distribution is different as measured by AFM and TEM, which suggests that the sample deposition process or grid-induced CNC clustering for TEM affects the measured CNC size distribution.

The difference between AFM height and TEM width for CNCs may be attributed to either an asymmetric cross-section or to agglomeration of CNCs that is not readily detectable by either imaging method. Addressing this question requires that width and height be measured for the same particles by one of the two methods. TEM of CNCs is challenging due to limited contrast, even after staining, so the option of using 3D TEM [19] seemed unlikely to resolve the issue. Therefore, we exploited our previous success in minimizing CNC aggregation using a fractionated sample and combined this with AFM imaging at low applied force and with a smaller (nominal) AFM tip radius for the best possible resolution. Accurate width and height measurements by AFM require that the measured width be corrected for AFM tip convolution effects. This can be accomplished by using an internal calibration standard (e.g., gold nanoparticles, AuNPs) to ensure the in-situ calibration of the AFM tip radius and to monitor changes in size. The measured width of individual CNCs by AFM can then be recalculated using this AFM tip radius. Garcia et al. [20] developed a mathematical procedure that was subsequently realized experimentally by Rowlen et al. [21] for determining the tip radius of an asymmetrical AFM probe by using relatively large (silica, 150 nm) and mid-sized (polystyrene, 50 nm) spherical nanoparticles. It was pointed out that this approach works best when the calibration sphere size is similar to the tip size [21].

An earlier study by Postek et al. [16] used in situ tip calibration standards to calibrate the size of CNCs by AFM. They analyzed the height and width distribution of 10 nm diameter AuNPs and calculated the AFM tip diameter by subtracting the mean height from the mean apparent width

assuming an aspect ratio of unity for the AuNPs. Here, we used a similar approach but with two sizes of gold nanoparticles (nominal diameters of 5 nm and 10 nm) for assessment of the tip radius, in order to fully cover the range of possible sizes of AFM probes used in the CNC imaging experiments. AuNPs and quantum dots have been extensively studied by AFM and shown to be appropriate for assessing tip size and structure [22-24]. The use of stable low force imaging is an important prerequisite for this work, in order to maintain image quality and minimize changes in the tip with imaging. This facilitates collection of a sufficient number of images to measure width and height for a statistically relevant number of CNCs. In our study, we have imaged fractionated CNCs with the two sizes of co-deposited AuNPs on freshly prepared poly-L-lysine coated mica. Each AuNP size is measured and calibrated individually. The AFM tip radius calculated from one size of AuNPs is validated with the second size of AuNPs before it is applied for CNC width calculation. A square or rectangular shape of the CNC cross-section is applied in our study as previous studies do not indicate a spherical cross-section for CNCs. The results indicate that the average CNC width is considerably larger than the average height, leading to estimates of a range of aspect ratios from < 1 to ≈ 3. We conclude that one-third of the CNCs in the fractionated samples have approximately symmetrical cross-sections in agreement with most models for the structure of the primary crystallite, whereas others are 2 or 3 laterally aggregated crystallites which have larger aspect ratios.

Materials and methods

Materials[1]

CNC (a National Research Council Canada certified reference material, CNCD-1, www.nrc.ca/crm) was dispersed at 2 % mass fraction in deionized water (18.2 MΩ cm at 25 °C) using a previously reported protocol [11]. Suspensions were sonicated with a total energy of 5000 J/g (130 W Cole Parmer ultrasonic processor, EW-04714-50, with a ¼ inch probe), stored at ≈ 5 °C

[1] The identification of any commercial product or trade name does not imply endorsement or recommendation by the National Institute of Standards and Technology or the National Research Council Canada.

and diluted prior to use. The hydrodynamic diameter was measured by dynamic light scattering (DLS, 0.05 % mass fraction in 5 mmol/L NaCl) using a Zetasizer Nano ZS (Malvern Panalytical, Westborough, MA) to verify that the dispersion properties were consistent with previous reports [11].

Asymmetrical-flow field-flow fractionation

This study utilized an AF4 system with an Eclipse3+ (Wyatt Technology, Santa Barbara, CA) coupled to a degasser (Gastorr TG-14, Flom Co., Ltd, Tokyo, Japan), an 1100-series isocratic pump (Agilent Technologies, Santa Clara, CA), a 1260 ALS series autosampler (Agilent), a multi-angle light scattering (MALS) detector (Dawn Heleos-II, Wyatt) with a laser at 661 nm and an online DLS detector at a scattering angle of 99.9° (Wyatt QELS, Wyatt). Fractionation and characterization were conducted for the CNCD-1 suspension using a mobile phase ionic strength of 1 mmol/L NaCl.

Using a previously developed AF4 method [17], two fractionated samples were collected from identically prepared CNC suspensions (CNCD-1,) both representing fraction 1 obtained at a retention time of (4 to 8) min: CNC-F1A (a replicate of sample “B3-F1” from our previous work [18]) and CNC-F1B (prepared and collected ≈ 4 months later).

Atomic force microscopy

Two types of CNC samples, CNCD-1 suspension and AF4 fractions CNC-F1A and B, were deposited on freshly cleaved mica for AFM imaging. For CNCD-1, a 2% mass fraction sonicated suspension was diluted 500-fold, vortex-mixed for 5 s, and spin-coated on a freshly poly-l-lysine (PLL) coated mica substrate. The method has been previously reported [11]. Briefly, a freshly cleaved mica substrate (diameter 12 mm, Ted Pella) was coated with 0.01% mass fraction PLL solution (Sigma-Aldrich) to provide a positively charged surface. A 25 µL aliquot of PLL solution was added onto the mica substrate, which was then covered with a petri dish for 15 min. The mica substrate was rinsed with deionized water five times and dried in a nitrogen stream. For spin coating, 30 µL of the freshly diluted CNCD-1 suspension was pipetted onto the center of the freshly prepared PLL-mica substrate, which was vacuum mounted onto a spin coater (WS-650SZ-6NPP/LITE, Laurel). The CNCD-1 suspension covered almost the entire substrate. The

spin coating was performed immediately using static mode at 4000 rpm (66.7 Hz) for 25 s, with an acceleration rate of 2000 rpm/s (33.3 Hz/s). The same AFM sample preparation was used for fractionated CNC samples without co-deposited AuNPs (Figure S1).

For the fractionated samples with co-deposited AuNPs, 140 µL aliquots of CNC-F1A and B (≈ 0.001% mass fraction) were each premixed with 35 µL of 15-fold diluted AuNPs-10 (EM.GC10, mean diameter 9.1 nm, *BBI Solutions*) and 35 µL of 20-fold diluted AuNPs-5 (EM.GC5, *BBI Solutions*, mean diameter 5.8 nm, provided by the supplier, *BBI Solutions*). All dilutions were performed with deionized water. Then, 50 µL of the mixture of CNC and AuNPs was pipetted onto a PLL coated mica substrate (similar as for CNCD-1), which was covered with a petri dish for 5 min. The sample was immersed in deionized water to remove excess CNC/AuNPs and immediately dried in a nitrogen stream. This sample preparation method gives an appropriate number and distribution of co-deposited AuNPs and CNCs.

CNC samples were imaged using a MultiMode AFM with a NanoScope V controller (Bruker Nano Surfaces Division, Santa Barbara, CA, USA) in PeakForce QNM mode. The use of PeakForce imaging facilitates stable and reproducible use of low (down to 10 pN) imaging force. Silicon nitride ScanAsyst-Air AFM probes (Bruker AFM Probes, Camarillo, CA) were used in all PeakForce imaging. The manufacturer specified nominal tip radius and spring constants are 2 nm ([25]) and 0.4 N/m, respectively, with three tip slopes: front angle of (15 ± 2.5)°, back angle of (25 ± 2.5)° and side angle of (17.5 ± 2.5)°. For a tip radius of 2 nm and a slope value of 25° the minimum particle radius is 1.3 nm. The maximum possible tip radius provided by the manufacture is 12 nm, which with a slope value of 25° yields a minimum particle radius of 7.8 nm [21]. Therefore, both 5 nm and 10 nm AuNPs are necessary for the full characterization of AFM probes and to obtain accurate values of the CNC width from AFM images. A series of (1 × 1) µm images were acquired with a resolution of (1024 × 1024) pixels at a scan rate of (0.7 to 0.8) Hz.

All AFM images were processed in Gwddyion 2.53 with align rows-median to remove skipping lines. The images were next flattened with first order leveling excluding masked CNCs and

AuNPs, after confirming that first and eleventh order flattening gave the same measured height.

Origin Pro was used for descriptive statistics. Particle size distributions are reported as the arithmetic mean and standard deviation as a measure of distribution width. Uncertainties are estimated as the 95% confidence interval calculated from the standard error of the mean with a coverage factor of 2.

Results

Initially, we examined an unfractionated sample of CNC using low imaging force (200 pN – 400 pN) and a smaller (nominal) tip radius than in our earlier work using conventional tapping mode AFM on a different microscope [11]. The image in Figure 1A shows a mixture of individual CNCs and small clusters or aggregates; individual CNCs can be clearly resolved in some of the aggregates. Individual CNCs were analyzed using our previous criteria for particle selection. Analysis of multiple images provide a mean CNC height of (3.3 ± 0.1) nm with a distribution width of 1.0 nm (calculated as the standard deviation) and a mean length of (67 ± 3) nm with a distribution width of 23 nm (n = 364). The particle size distribution is illustrated in Figure 1B as a 2D kernel density plot. The mean height and length are in good agreement with our previous results (mean height and length of (3.4 ± 0.1) nm and (77 ± 2) nm, respectively) which were based on analysis of a larger number (x 5) of particles from multiple samples imaged with a larger AFM tip radius (nominal value of 8 nm, HQ:XSC11 AL BS). The similar heights measured in the two experiments support our previous conclusion that compression by the AFM tip at the imaging force used contributes at most 0.19 nm to the uncertainty in measured height; this means that compression of the CNCs by the AFM tip cannot account for the observed difference between TEM width and AFM height [11]. The ability to image reproducibly at low applied force improves the image quality and allows acquisition of multiple AFM images without significant tip wear and the resulting deterioration of image quality.

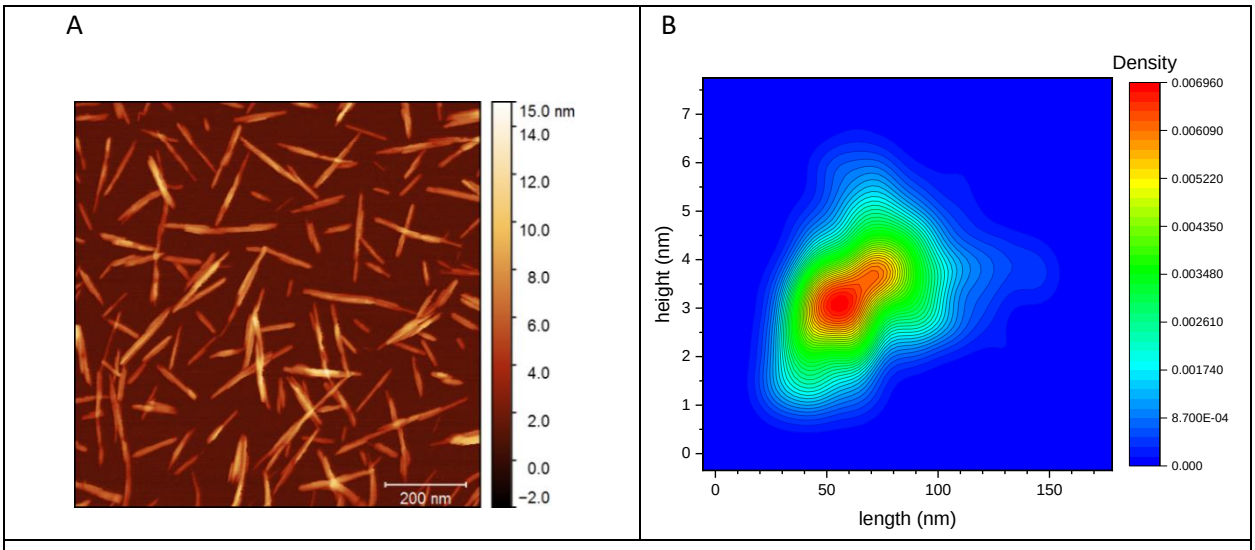

Figure 1: PeakForce AFM imaging of CNCD-1 (A) and the 2D-Kernel density plot showing the height and length particle size distribution (B).

Having established that imaging at low applied force with nominally smaller tip size gave similar results to our previous CNC imaging, we next imaged CNC samples that were fractionated by AF4. We imaged the first fraction collected by AF4 (CNC-F1A) which previous work had shown to contain the lowest percentage of clustered CNCs [18]. This sample had an estimated length of 111 ± 10 nm from the MALS detector signal (Figure S1) and using the rod model in good agreement with results (113 ± 12 nm) for a replicate sample prepared at the same time in the previous study. Figure S1 shows an AFM image for this sample obtained by PeakForce AFM imaging with a similar sample preparation (30 µL of CNC-F1A); the particle density and the number of clusters/aggregates is much lower than for the unfractionated sample (Figure 1). To check for reproducibility, a second fractionated sample (CNC-F1B) prepared using the same AF4 method, gave a rod length of (108 ± 18) nm based on MALS, although the fractogram (Figure 2A) showed some differences in later fractions compared to sample CNC-F1A. The AFM images for CNC-F1B (Figure 2B, C) clearly illustrate the ability to resolve two laterally aggregated CNCs. The height profile (Figure 2C) shows two individual CNCs with heights of ≈ 4.6 nm and ≈ 4.2 nm for profiles #1 and #2, respectively. Their corresponding overall apparent widths are ≈ 17 nm and ≈ 18 nm. Small dips on the height profiles indicate that the separation between the two particles is just at the limit of the AFM resolution.

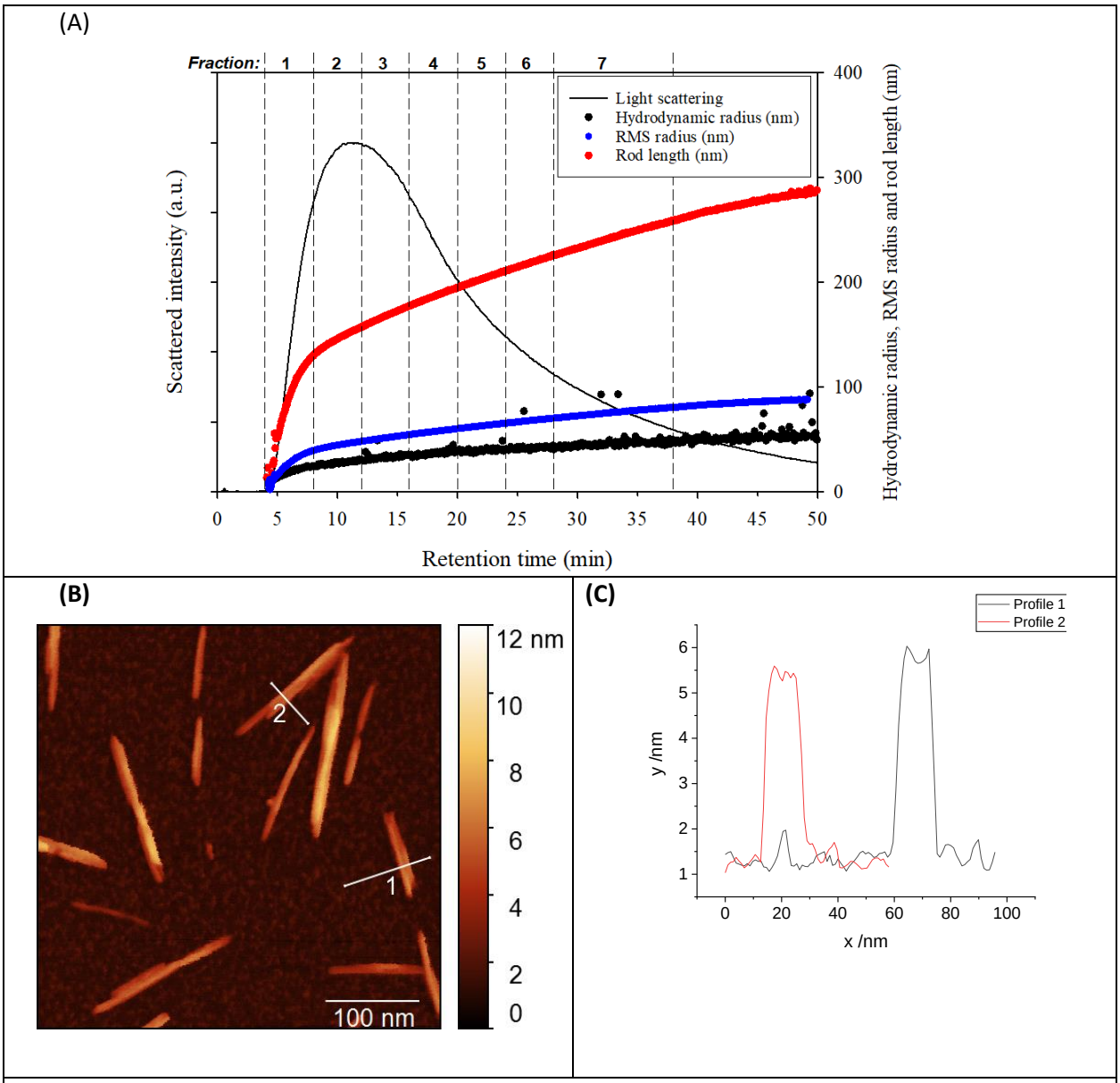

Figure 2: AF4 fractogram (A) and AFM image (B) for sample CNC-F1B with cross-sections (C) for the two marked features in the AFM image.

Fractionated CNC was co-deposited with two sizes of AuNPs with nominal diameters of 5 nm and 10 nm. Figure 3A shows a representative image obtained for CNC-F1B, with a cross-section illustrating the small and large AuNPs along with an individual CNC. Note the relatively high fraction of individual CNCs despite the higher overall particle density compared to the image in

Figure 2A. The first sample, CNC-F1A (a replicate prepared during the previous study [18]), yielded similar results.

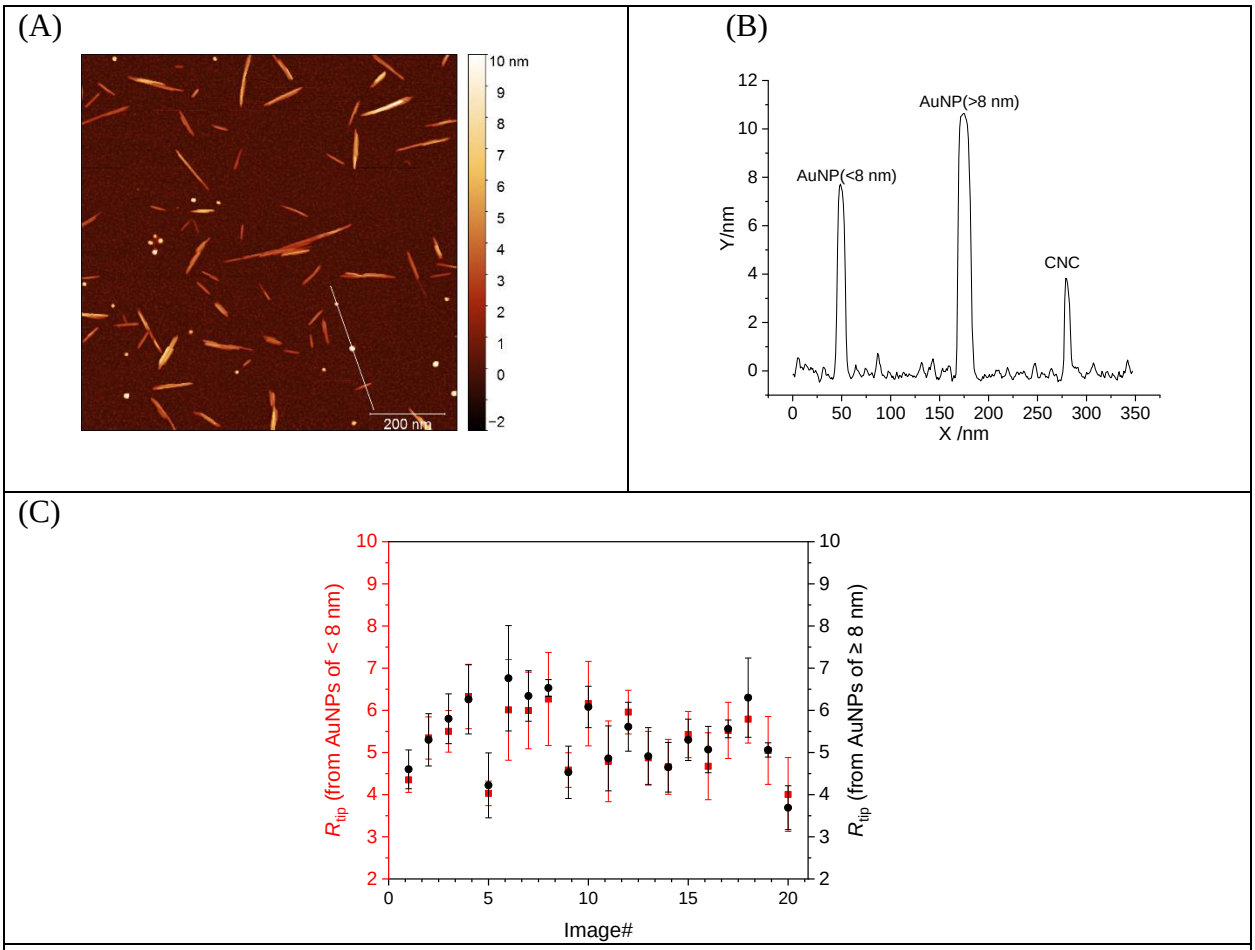

Figure 3: Representative AFM image of CNC-F1B with co-deposited AuNPs (A) and a cross-section showing two sizes of AuNPs and an individual CNC (B); AFM tip radii (C) estimated from two sizes of AuNPs, < 8 nm and ≥ 8 nm. The AFM tip radii are in units of nm with error bars of standard deviation and are for all images for CNC-F1A and CNC-F1B.

Prior to measuring CNC height and width for the fractionated samples, we measured both heights and widths of the co-deposited AuNPs in order to estimate the tip radius. With two sizes of AuNPs, we can select certain sizes of AuNPs for the estimation of the AFM tip radius (R_{tip}); the remainder of the AuNPs can be used for internal validation of the AFM tip radius. Assuming a spherical shape for the AuNPs and minimal compression of the AuNPs by the AFM tip, one can reasonably estimate the AFM tip radius [24, 26, 27] using *Eq.1*, with an

approximation of the half cone angle of 20° for the AFM tip and a tip radius (R_{tip}) less than or comparable to the height (H_{Au}) of AuNPs.

$$R_{tip} = \frac{W_{\exp\_Au}^2}{8H_{Au}} \qquad Eq.\ (1)$$

H_{Au} and particle width (W_{exp_Au}) values were measured from the cross-section profiles of each individual AuNP. Four cross-section profiles separated by 45 degree angles were drawn across the maximum height of a given AuNP and the average value was calculated for both height and width (Figure 3B). The height was measured as the difference between the vertical maxima of each profile, ignoring any single point spikes, and the adjacent background. For the width measurement, the slopes defined by the first few points that deviate from the background level on either side of the profile were extrapolated to intersect the background level. The distance between the two intersection points was measured to give the width. AuNPs that are touching, on the edge of the AFM image, or visually non-spherical/distorted were excluded. First, we arbitrarily selected AuNPs with heights of less than 8 nm for the estimation of the AFM tip radii. In total, 139 AuNPs (< 8 nm) were analyzed from all images for the 2 samples, which resulted in an average tip size for each of the 20 AFM images ranging from (4 to 7) nm, see Figure 3C. It should be noted that multiple tips were used for the experiment.

To validate the estimated AFM tip radius, $W_{\mathrm{Cal\_Au}}$ of 133 AuNPs (≥ 8 nm) was then calculated using *Eq.2*. $W_{\mathrm{Cal\_Au}}$ value is the calculated width of AuNPs after accounting for the AFM tip broadening.

$$W_{\mathrm{Cal\_Au}} = W_{\mathrm{Exp\_Au}} - (\sqrt{8 * R_{\mathrm{tip}} * H_{\mathrm{Au}}} - H_{\mathrm{Au}}) \qquad -Eq.\ (2)$$

Assuming minimum compression of the particles during the AFM measurements, the ratio of $W_{\mathrm{Cal\_Au}}$ and H_{Au} represents the aspect ratio of the AuNPs (> 8nm), which is shown in Figure 4A. The aspect ratio values for these 133 AuNPs (≥ 8 nm) mainly fall within the 0.8-1.3 range (mean of 1.02 with a standard deviation of 0.14); this validates the approach for estimating the tip radius since a spherical AuNP will have a ratio of $W_{\mathrm{Cal\_Au}}$ to H_{Au} of 1.

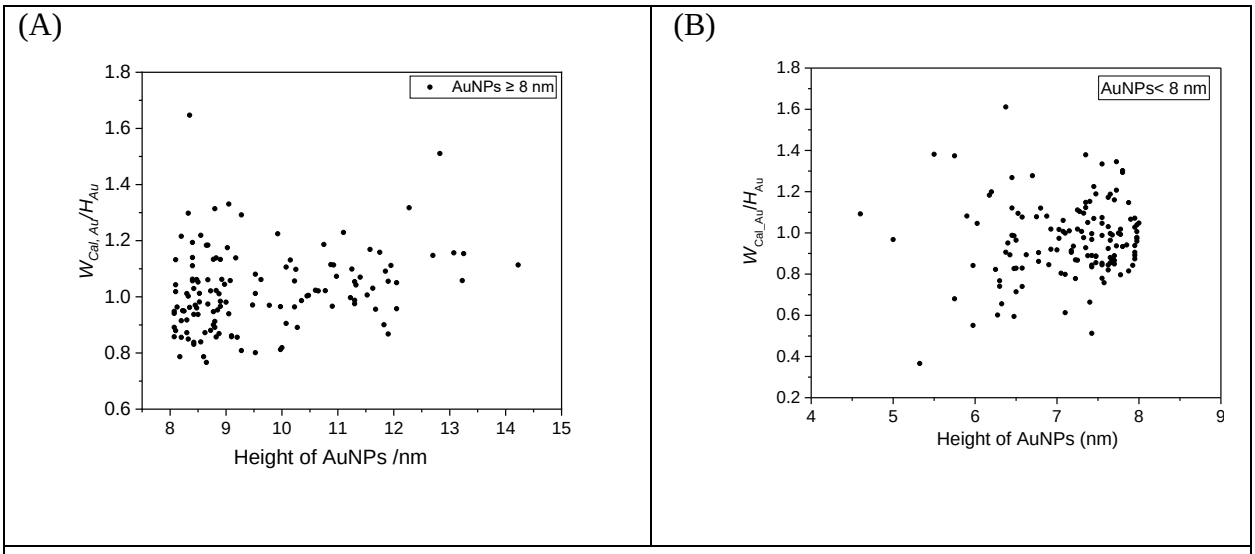

Figure 4: Aspect ratio of the AuNPs with the height of ≥ 8 nm (A) and < 8 nm (B) plotted against AuNP height.

The same approach was repeated using AuNPs (≥ 8nm) from the same images for estimation of the AFM tip radius. The ratios of $W_{Cal_Au}$and H_{Au} of AuNPs (< 8 nm) mainly fall within the 0.6-1.4 range (Figure 4B), which is slightly broader than that using AuNPs (< 8 nm) for the AFM tip estimation. Nevertheless, the mean ratio is 0.97 with a standard deviation of 0.18. This result also indicates an aspect ratio of 1 for AuNPs (< 8nm).

The AFM tip radius calculated from the AuNP measurements described above was then used to calculate the CNC width. We initially applied the surface reconstruction method in Gwyddion to deconvolute the AFM images. The average tip radius obtained for all AuNPs in a specific image was used for the deconvolution of that image. This was an attempt to directly extract the height and width values of CNC from the deconvoluted AFM images. However, it was found that the surface reconstruction method altered the CNC height by ≈ (0.5 to 1) nm (Figure S2), possibly due to the algorithm and models used in this method. To overcome the complexity of the modeling/calculating algorithm used in the Gwyddion surface reconstruction, we measured height (H_{CNC}) and width ($W_{\mathrm{exp\_CNC}}$) values of individual CNCs after taking account of the AFM tip convolution using two internal calibration AuNPs in our current study. The height and width of individual CNCs are measured from a single transverse profile at the maximum CNC width

(Figure 5A), perpendicular to its long axis. Assuming a square or rectangular shape as suggested by models of the primary crystallites of wood pulp CNCs [5, 28], the calculated width of CNCs ($W_{\mathrm{Cal\_CNC}}$) can be determined using Eq. 3 [26, 29]:

$$W_{\mathrm{Cal\_CNC}} = W_{\mathrm{exp\_CNC}} - 2 \times \sqrt{2R_{\mathrm{tip}}H_{\mathrm{CNC}} - H_{\mathrm{CNC}}^2} \qquad Eq.\ (3)$$

Thus, the ratios between calculated width and measured height values can be used to determine the symmetry of CNCs.

The above procedure was repeated for the two fractionated CNC samples. The results are summarized as histograms of W_{Cal_CNC}/H_{CNC} for the combined set of 307 CNCs using the < 8 nm AuNPs and ≥ 8 nm AuNPs for estimating the tip radius (Figure 5 B, C). The data based on the two estimates of tip radius are not significantly different at the 0.05 level as assessed by a Kolmogorov-Smirnov test for similarity of the two distributions. However, there are small differences between samples CNC-F1A and CNC-F1B as shown in Figure S3, which provides histograms for calculated width and height for the two fractionated samples and the combined sample. Although the same mean height is obtained for the two samples, the calculated width varies, with mean values of 5.8 nm and 4.4 nm for CNC-F1A and CNC-F1B, respectively. The measured lengths (Figure S4) are similar for the two samples, in agreement with the estimates from the MALS data collected during the AF4 fractionation, 111 ± 10 nm for CNC-F1A and 108 ± 18 nm for CNC-F1B. Note that changes in the CNC dimensions for the two AF4 samples may reflect one or more of the following: small variations in the initial CNC suspensions used for fractionation (which were prepared in different laboratories); differences in AF4 separation conditions; the length of storage time for the fractionated samples (CNC-F1A was used several months after preparation whereas CNC-F1B was used within several weeks); and the method for calculating the CNC width. Since both samples showed that the CNC width was considerably larger than height, further discussion focuses on the combined data set.

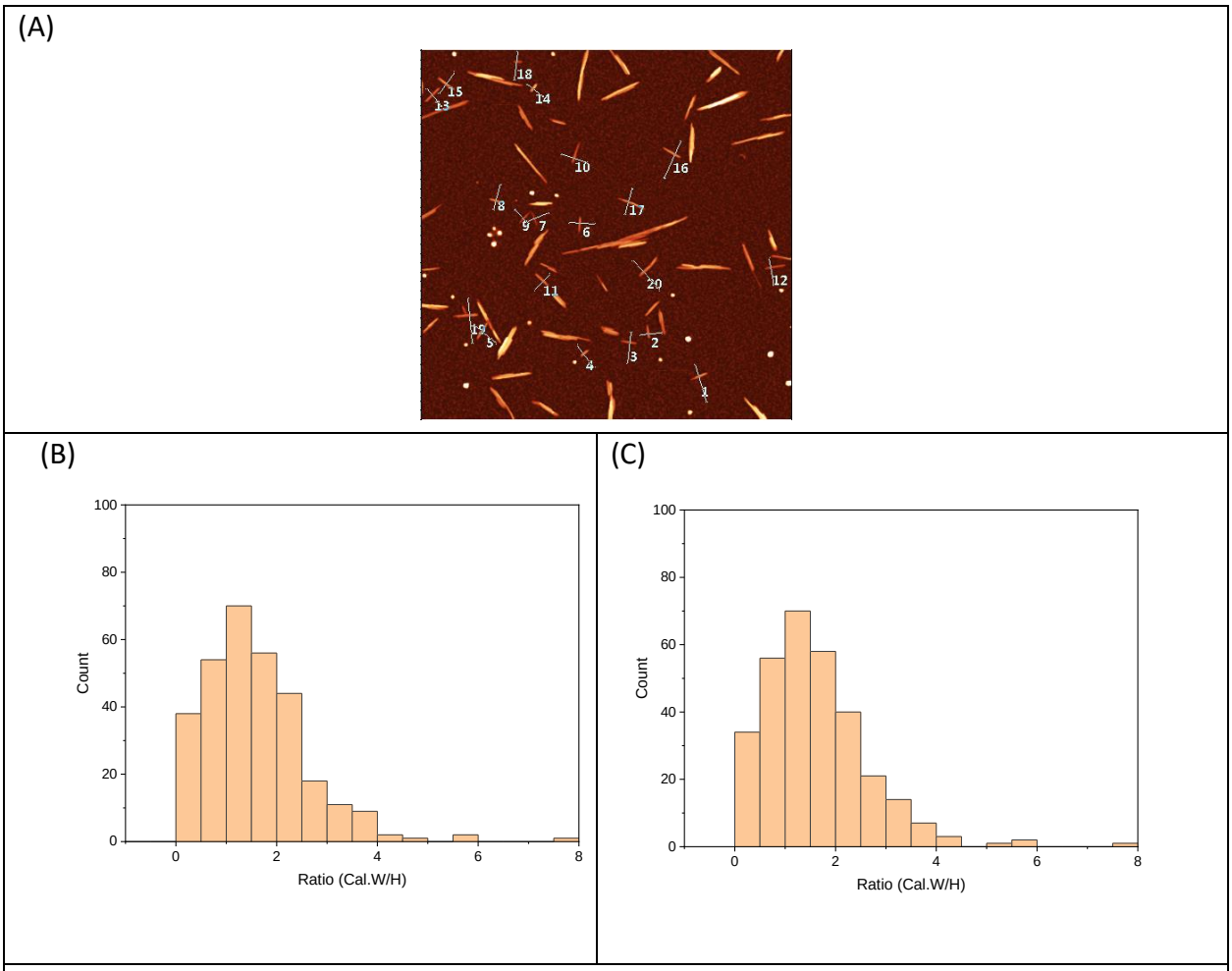

Figure 5: AFM image (A) for CNC-F1B showing CNCs selected for width and height measurements; (B, C) Ratio of height/width for the combined data set for the fractionated CNC samples measured using AuNPs with heights of ≥ 8 nm and < 8 nm, respectively.

The width/height ratio for fractionated CNC samples (Figure 5) varies over a relatively wide range compared to the measurements for the AuNPs. Most of the CNCs have their wider side (long axis in a cartoon in Figure 6) adsorbed to the PLL-coated mica substrate (width/height >1) while a minority (≈ 31 %, width/height <1) have their shorter side adhering to the substrate. The calculated width/height ratios were converted to an aspect ratio for the CNC cross-section (AR, defined as the ratio of the larger value and the smaller value of the calculated width and height,) which is displayed as a histogram in Figure S5. A fraction (≈ 28 %) of the measured

CNCs have an approximately symmetric cross-section, defined as an aspect ratio between 1 and 1.4 and ≈ 62% have aspect ratios between 1.4 and 3.4.

The correlation of calculated CNC width with height is shown in the scatter plot in Figure 6; the AuNPs with heights ≥ 8 nm were used to estimate the CNC width and the equivalent plot using AuNPs with heights < 8 nm (Figure S6) shows very similar results. The CNCs with aspect ratio < 1.4 (red) show a correlation between the calculated width and height with a slope of approximately 1. There is also a population of particles for which the width axis is approximately twice the height (slope of ≈ 2) and a smaller number with aspect ratios as large as 3-4. The black points near the x-axis in Figure 6 correspond to the population of CNCs that are adsorbed with their short axis on the substrate (i.e., calculated width is less than measured height). These results indicate a clear correlation of width and height after the different populations are taken into account.

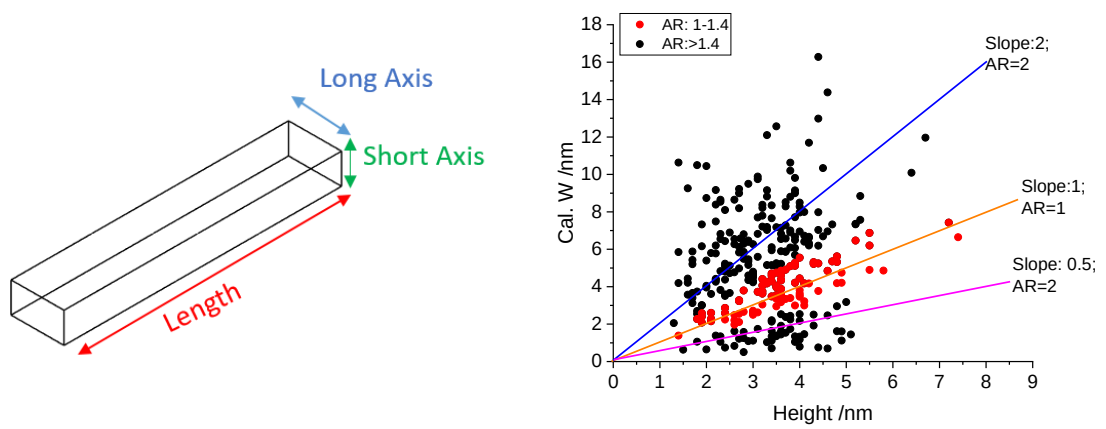

Figure 6. Cartoon (left) illustrating the short and long axis for the CNC cross-section. Scatter plot (right) showing the correlation between calculated width and measured height for fractionated CNCs (combined data set for CNC-F1A and CNC-F1B). CNCs with an aspect ratio for the cross-section between 1 and 1.4 are shown in red. The solid lines are a visual aid to illustrate the correlation between width and height for CNCs with different aspect ratios. AuNPs with heights ≥ 8 nm were used to calculate CNC widths.

Discussion and Conclusions

AFM measurements of AuNPs as internal calibration standards were employed for *in situ* measurements of AFM tip radius, facilitating calculation of the CNC width. The use of fractionated CNC samples with a low number of clustered CNCs was essential for the success of these measurements. These experiments also took advantage of the improved AFM image quality with low applied force and small tip radius and used two sizes of AuNPs to cover the range of possible tip geometries and provide internal validation of the method for estimating the tip radius. The results indicate that there is a population of CNCs that have an approximately symmetrical cross-section whereas the remainder have one axis of the cross-section that is 2-3 times longer than the other. Both AFM and TEM have been widely used to measure CNC size; both methods provide length data, with TEM providing an estimate of cross-section based on particle width and AFM providing particle height [5, 8, 30]. Most published studies have not considered possible differences between cross-section measurements obtained from the two methods, an observation that may be related to the initial models for the CNC structure. Early models for the elementary fibrils of plant-derived CNCs were based on a 6 x 6 array of polymer chains assembled during biosynthesis by a rosette-shaped terminal enzyme complex with six-fold symmetry [5, 31]. Individual fibrils were considered to have a square geometry with dimensions that range between 3 nm and 5 nm; the estimates were typically based on X-ray diffraction data and varied somewhat for different studies and different types of plant-derived CNCs [32-34]. By contrast, CNCs from other (non-plant) based sources (e.g., tunicates and bacteria) assembled to yield rectangular, ribbon-like structures that were presumably determined by the linear structure of the terminal complex used in biosynthesis. More recent studies provide a range of other estimates for the number of subunits in plant-based fibrils produced by the terminal enzyme complex [32, 35]. Estimates vary from 18 to 36 subunits and a variety of geometries are suggested, including diamond, parallelogram and hexagonal arrangements. For example, a diamond geometry with dimensions of 3.2 nm and 3.9 nm and a rectangular geometry with dimensions of 3.2 nm and 3.1 nm is proposed based on X-ray scattering and small-angle neutron scattering (SANS) data [32]. Regardless of the number of possible geometries, various studies using X-ray scattering, solid-state NMR and SANS all

indicate that the cross-sectional dimensions of plant-derived CNCs fall within the range of (3 to 5) nm, with differences of (20 to 30) % in the two cross-section dimensions.

To-date there are relatively few studies that have attempted to correlate cross-sectional width and height for the same sample for wood and other plant-derived CNCs. As noted in the introduction, AFM and TEM measurements of cotton-derived CNCs indicate a rectangular cross-section that is attributed to aggregation of individual crystallites. Similar results have been reported for CNCs prepared from sulfuric acid hydrolysis of switchgrass [14]. By contrast, a study on wood-pulp CNCs used a deconvolution method similar to that described above to obtain AFM height and width measurements that were similar (6.4 nm and 7.8 nm for height and width, respectively) [16]. An electron tomography study provided evidence that the three-dimensional structure of CNCs produced from filter paper has a rectangular cross-section (5-10 nm and 18-40 nm for the long and short axes, respectively) although the low sensitivity and potential for beam damage makes this a challenging experiment [19]. The latter two studies appear to be the only examples in which both cross-sectional dimensions have been obtained for the same particles (as opposed to the same sample, but using different sample preparation and imaging methods). However, it is worth noting that in both cases the dimensions of the particles are larger than the primary crystallite measurements from other techniques, indicating that the CNC samples contained particles with multiple crystallites.

The mean height of 3.3 nm measured here for the fractionated CNCs is in good agreement with the expected dimensions of the primary fibrils produced by the enzyme complex. The calculated widths indicate that ≈ 28% of the CNCs have aspect ratios that are approximately symmetric and ≈ 63 % have aspect ratios in the range of 1.4 – 3.4 (Figure 6). The results are similar for two independently prepared fractionated samples. There is also a clear correlation between the width obtained after deconvolution (using Eq. 3) and the measured height for each of these populations. The considerably longer dimensions for the width cross-section could be due to several factors. First, as noted above, some recent models postulate an asymmetric cross-section. Although this may account for some of the width variation observed, none of the proposed models predict CNCs with an aspect ratio between 2 and 3. Strong lateral aggregation of CNCs that is promoted by hydrogen bonding is a second possibility and is

consistent with some previous reports. For example, SANS measurements of CNCs indicate that lateral aggregation of CNCs occurs in a concentration-dependent manner [28, 36]. TEM has been suggested to lead to aggregates, in some cases induced by staining that is necessary to achieve adequate image contrast for size measurements [37]. An alternate possibility is that the hydrolysis process that generates the CNCs does not completely remove amorphous cellulose that could serve to bind primary crystallites together. Although this certainly accounts for observations of considerably larger particles for samples subjected to a shorter hydrolysis times or lower acid concentration or temperature, it seems unlikely that incomplete hydrolysis of amorphous cellulose would lead to laterally aggregated particles Therefore we conclude that inherent lateral aggregation of crystals is the predominant reason for the large asymmetry in cross-section. It should be noted that the presence of laterally aggregated particles is always accompanied by the presence of unstructured clusters of CNCs for unfractionated samples. Finally, the relatively broad particle size distributions measured for both height and width make it impossible to distinguish between the various models that have been proposed for CNC structures.

Supporting information

Additional figures summarizing the attempted Gwyddion deconvolution and histograms for the fractionated CNC samples.

Acknowledgments

We acknowledge Arnab Mukherjee (formerly of NIST) for his contributions to the development of methods for AF4 fractionation of CNC.

References

1. Dufresne, A. Nanocellulose processing properties and potential applications. *Current Forestry Reports* 2019, 5, 76-89.
2. Eichhorn, S. Cellulose nanowhiskers: Promising materials for advanced applications. *Soft Matter* 2011, 7, 303-315.
3. Jorfi, M., Foster, E. J. Recent advances in nanocellulose for biomedical applications. *J. Appl. Polym. Sci.* 2015, 2015, 41719.
4. Klemm, D., Kramer, F., Moritz, S., Lindstrom, T., Ankerfors, M., Gray, D., Dorris, A. Nanocelluloses: A new family of nature-based materials. *Angew. Chem. Int. Ed. Engl.* 2011, 50, 5438-5466.
5. Moon, R. J., Martini, A., Nairn, J., Simonsen, J., Youngblood, J. Cellulose nanomaterials review: Structure, properties and nanocomposites. *Chem. Soc. Rev.* 2011, 40, 3941-3994.
6. Shatkin, J. A., Wegner, T. H., Bilek, E. M., Cowie, J. Market projections of cellulose nanomaterial-enabled products- part 1: Applications. *TAPPI J.* 2014, 13, 9-16.
7. Thomas, B., Raj, M. C., Athira, K. B., Rubiyah, M. H., Joy, J., Moores, A., Drisko, G. L., Sanchez, C. Nanocellulose, a versatile green platform: From biosources to materials and their applications. *Chem. Rev.* 2018, 118, 11575-11625.
8. Foster, E. J., Moon, R. J., Agarwal, U. P., Bortner, M. J., Bras, J., Camarero-Espinosa, S., Chen, K. J., Clift, M. J. D., Cranston, E. D., Eichhorn, S. J., Fox, D. M., Hamad, W. Y., Heux, L., Jean, B., Korey, M., Nieh, W., Ong, K. J., Reid, M. S., Renneckar, S., Roberts, R., Shatkin, J. A., Simonsen, J., Stinson-Bagby, K., Wanasekara, N., Youngblood, J. Current characterization methods for cellulose nanomaterials. *Chem. Soc. Rev.* 2018, 47, 2609-2679.
9. Davis, C. S., Moon, R. J., Ireland, S., Foster, E. J., Johnston, L. J., Shatkin, J. A., Nelson, K., Forster, A. M., Postek, M. T., Vladar, A. E., Gilman, J. W., *NIST-TAPPI workshop on measurement needs for cellulose nanomaterials*. 2015. p. DOI 10.6028/NIST.SP.1192.
10. Brinkmann, A., Chen, M., Couillard, M., Jakubek, Z. J., Leng, T., Johnston, L. J. Correlating cellulose nanocrystal particle size and surface area *Langmuir* 2016, 32, 6105-6114.
11. Jakubek, Z. J., Chen, M., Couillard, M., Leng, T., Liu, L., Zou, S., Baxa, U., Clogston, J. D., Hamad, W., Johnston, L. J. Characterization challenges for a cellulose nanocrystal reference material: Dispersion and particle size distributions *J. Nanopart. Res.* 2018, 20, 98.
12. Mazloumi, M., Johnston, L. J., Jakubek, Z. J. Dispersion, stability and size measurements for cellulose nanocrystals by static multiple light scattering. *Cellulose* 2018, 25, 5751-5768.
13. Elazzouzi-Hafraoui, S., Nishiyama, Y., Putaux, J.-L., Heux, L., Dubreuilf, F., Rochas, C. The shape and size distribution of crystalline nanoparticles prepared by acid hydrolysis of native cellulose. *Biomacromolecules* 2008, 9, 57-65.

14. Meng, Y., Wu, Q., Young, T. M., Huang, B., Wang, S., Li, Y. Analyzing three-dimensional structure and geometrical shape of individual cellulose nanocrystal from switchgrass. *Polymer Composites* 2017, 2368-2377.
15. Brito, B. S. L., Pereira, F. V., Putaux, J.-L., Jean, B. Preparation, morphology and structure of cellulose nanocrystals from bamboo fibers. *Cellulose* 2012, 19, 1527-1536.
16. Postek, M. T., Vladar, A., Dagata, J., Farkas, N., Ming, B., Wagner, R., Raman, A., Moon, R. J., Sabo, R., Wegner, T. H., Beecher, J. Development of the metrology and imaging of cellulose nanocrystals. *Meas. Sci. Tech.* 2011, 22, 024005.
17. Mukherjee, A., Hackley, V. A. Separation and characterization of cellulose nanocrystals by multi-detector asymmetric flow field-flow fractionation. *Analyst* 2017, 143, 731-740.
18. Chen, M., Parot, J., Mukherjee, A., Couillard, M., Zou, S., Hackley, V. A., Johnston, L. J. Characterization of size and aggregation for cellulose nanocrystal dispersions separated by asymmetrical-flow field-flow fractionation. *Cellulose* 2020, 27, 2015-2028.
19. Majoinen, J., Haataja, J. S., Appelhans, D., Lederer, A., Olszewska, A., Seitsonen, J., Aseyev, V., Kontturi, E., Rosilo, H., Österberg, M., Houbenov, N., Ikkala, O. Supracolloidal multivalent interactions and wrapping of dendronized glycopolymers on native cellulose nanocrystals. *J. Am. Chem. Soc.* 2014, 136, 866-869.
20. Garcia, V. J., Martinez, L., Briceno-Valero, J. M., Schilling, C. H. Dimensional metrology of nanometric spherical particles using AFM. *Probe Microscopy* 1997, 14, 107-116.
21. Ramirez-Aguilar, K. A., Rowlen, K. L. Tip characterization from AFM images of nanometric spherical particles. *Langmuir* 1998, 14, 2562-2566.
22. Ebenstein, Y., Nahum, E., Banin, U. Tapping mode atomic force microscopy for nanoparticle sizing: Tip−sample interaction effects. *Nano Lett.* 2002, 2, 945-950.
23. Taaties, D. J., Quinn, A. S., Lewis, M. R., Bovill, E. G. Quality assessment of atomic force microscopy probes by scanning electron microscopy: Correlation of tip structure with rendered images. *Micros. Res. Tech* 1999, 44, 312-326.
24. Vesenka, J., Manne, S., Giberson, R., Marsh, T., Henderson, E. Colloidal gold particles as an incompressible atomic force microscope imaging standard for assessing the compressibility of biomolecules. *Biophys. J.* 1993, 65, 992-997.
25. Slattery, A. D., Shearer, C. J., Shapter, J. G., Blanch, A. J., Quinton, J. S., Gibson, C. T. Improved application of carbon nanotube atomic force microscopy probes using peakforce tapping mode. *Nanomaterials* 2018, 8, 807.
26. Canet-Ferrer, J., Coronado, E., Forment-Aliaga, A., Pinilla-Cienfuegos, E. Correction of the tip convolution effects in the imaging of nanostructues studied through scanning force microscopy. *Nanotechnology* 2014, 25, 395703.

27. Maeda, H. An atomic force microscopy study for the assembly structures of tobacco mosaic virus and their size evaluation. *Langmuir* 1997, 13, 4150-4161.
28. Uhlig, M., Fall, A., Wellert, S., Lehmann, M., Prévost, S., Wågberg, L., von Klitzing, R., Nyström, G. Two-dimensional aggregation and semidilute ordering in cellulose nanocrystals. *Langmuir* 2016, 32, 442-450.
29. Goken, M., Kempf, M. Microstructural properties of superalloys investigated by nanoindentations in an atomic force microscope. *Acta Mater.* 1999, 47, 1043-1052.
30. ISO 19716:2016 Characterization of cellulose nanocrystals
31. Brown, R. M. The biosynthesis of cellulose. *Pure Appl. Chem.* 1996, A33, 1345-1373.
32. Fernandes, A. N., Thomas, L. H., Altaner, C. M., Callow, P., Forsyth, V. T., Apperley, D. C., Kennedy, C. J., Jarvish, M. C. Nanostructure of cellulose microfibrils in spruce wood. *Proc. Natl. Acad. Sci.* 2011, 108, E1195-E1203.
33. Hamad, W. Y., Hu, T. Q. Structure-property-yield inter-relationships in nanocrystalline cellulose extraction *Can. J. Chem. Eng.* 2010, 88, 392-402.
34. Jiang, F., Esker, A. R., Roman, M. Acid-catalyzed and solvolytic desulfation of H_2SO_4-hydrolyzed cellulose nanocrystals. *Langmuir* 2010, 26, 17919-17925.
35. Wang, T., Hong, M. Solid-state nmr investigations of cellulose structure and interactions with matrix polysaccharides in plant primary cell walls. *J. Exp. Botany* 2016, 67, 503-514.
36. Cherhal, F., Cousin, F., Capron, I. Influence of charge density and ionic strength on the aggregation process of cellulose nanocrystals in aqueous suspension, as revealed by small-angle neutron scattering. *Langmuir* 2015, 31, 5596-5602.
37. Kaushik, M., Chen, W. C., van de Ven, T. G. M., Moore, A. An improved methodology for imaging cellulose nanocrystals by transmission electron microscopy. *Nordic Pulp & Paper Res. J.* 2014, 29, 77-84.